APPLIED PHYSICS

Nanoscale optical writing through upconversion resonance energy transfer

S. Lamon[1,2], Y. Wu[3], Q. Zhang[1], X. Liu[3,4], M. Gu[1,2]*

Nanoscale optical writing using far-field super-resolution methods provides an unprecedented approach for high-capacity data storage. However, current nanoscale optical writing methods typically rely on photoinitiation and photoinhibition with high beam intensity, high energy consumption, and short device life span. We demonstrate a simple and broadly applicable method based on resonance energy transfer from lanthanide-doped upconversion nanoparticles to graphene oxide for nanoscale optical writing. The transfer of high-energy quanta from upconversion nanoparticles induces a localized chemical reduction in graphene oxide flakes for optical writing, with a lateral feature size of ~50 nm (1/20th of the wavelength) under an inhibition intensity of 11.25 MW cm^{-2}. Upconversion resonance energy transfer may enable next-generation optical data storage with high capacity and low energy consumption, while offering a powerful tool for energy-efficient nanofabrication of flexible electronic devices.

INTRODUCTION

In the Data Age, high-density optical data writing is a key technology to store information (*1*). Multiplexed digital data storage in quartz glass has marked the rebirth of optical data storage for big data (*2*, *3*). However, femtosecond laser nanostructuring of fused quartz glass prevents energy-efficient optical writing at the nanometer scale needed for sustainable optical clouds. Nanoscale optical writing using far-field super-resolution methods provides an unprecedented approach for high-capacity data storage (*4*, *5*). However, current nanoscale optical writing methods typically rely on photoinitiation and photoinhibition with high beam intensity, high energy consumption, and short device lifetime (*6*–*14*).

Lanthanide-doped upconversion nanoparticles (UCNPs) (*15*), which can optically convert a low-energy near-infrared beam into high-energy ultraviolet (UV) or visible photons, have facilitated photoactivation in lithography (*16*), theranostics (*17*), photoswitching (*18*), optogenetics (*19*), and optical memory (*20*). Furthermore, UCNPs exhibit long-lived excited energy levels for reduced transition rates compared with organic fluorophores, enabling low-power stimulated emission depletion (STED) microscopy (*21*, *22*). Thus, we reasoned that localized control of electronic transitions in UCNPs through far-field super-resolution methods would allow energy transfer–driven, low-power photoactivation for optical writing beyond the diffraction resolution barrier.

Here, we demonstrate nanoscale optical writing using UCNPs and graphene oxide (GO) (*23*) as the substrate. Our approach involves the resonance energy transfer (RET) (*24*) of high-energy quanta from UCNPs to induce a localized chemical reduction in GO flakes. Using dual-beam super-resolution irradiation, we achieve optical writing of features with a lateral feature size of ~50 nm (1/20th of the wavelength) under an inhibition intensity of 11.25 MW cm^{-2}. Furthermore, we exploit quenching of upconversion luminescence by the formed reduced GO (rGO) for high-contrast subdiffraction optical readout of the written features, which lays the potential for nanoscale all-optical memory.

RESULTS

The principle of RET-assisted (RETA) optical writing on a GO-conjugated UCNP substrate is illustrated in Fig. 1. We used one 980-nm beam for writing through GO reduction to rGO, assisted by RET of high-energy quanta generated in UCNPs by optical upconversion of near-infrared light (Fig. 1A). We used a second 808-nm beam for inhibition of GO reduction by preventing high-energy quantum generation in UCNPs through de-excitation of intermediate excited states. This optical writing differs from those diffraction-limited methods through photothermal or photochemical processes because of uncontrolled GO reduction (*25*). RETA optical writing allows one to fabricate subdiffraction features on nanocomposite substrates by shaping the inhibition beam into a doughnut with zero intensity at the central point (Fig. 1B).

Many combinations of light-sensitive materials are suitable as RET donor-acceptor pairs for nanoscale RETA optical writing, wherein the subdiffraction feature size depends on the intensity of the inhibition beam and the saturation intensity of the material. The advantages of using GO-conjugated UCNPs are (i) UCNPs generate localized high-energy quanta, which enables GO reduction with high spatial confinement for nanoscale optical writing; (ii) UCNPs have long-lived excited states with reduced transition rates, which enables low-power inhibition using continuous-wave (CW) laser sources; and (iii) GO can undergo reduction to rGO, which provides a convenient pathway for energy-efficient nanofabrication of devices based on graphene-like materials.

Figure 1C shows the normalized intensity distribution of the 980-nm writing beam with a Gaussian shape (writing), the 808-nm inhibition beam with a doughnut shape (inhibition), and their spatial overlap (writing + inhibition) along the radial direction in the focal plane, simulated through the vectorial Debye theory for a high numerical aperture (NA) objective (*26*). UCNP-induced GO reduction is confined to a subdiffraction region at the central point of the doughnut. In a proof-of-principle experiment, subdiffraction features were fabricated on the nanocomposite through RETA optical writing (Fig. 1, D and E, and fig. S1). The resulting subdiffraction

---

[1]Centre for Artificial-Intelligence Nanophotonics, School of Optical-Electrical and Computer Engineering, University of Shanghai for Science and Technology, Shanghai 200093, China. [2]Laboratory of Artificial-Intelligence Nanophotonics, School of Science, RMIT University, Melbourne 3001, Australia. [3]Department of Chemistry, National University of Singapore, Singapore 117543, Singapore. [4]The N.1 Institute for Health, National University of Singapore, Singapore 117456, Singapore.
*Corresponding author. Email: gumin@usst.edu.cn

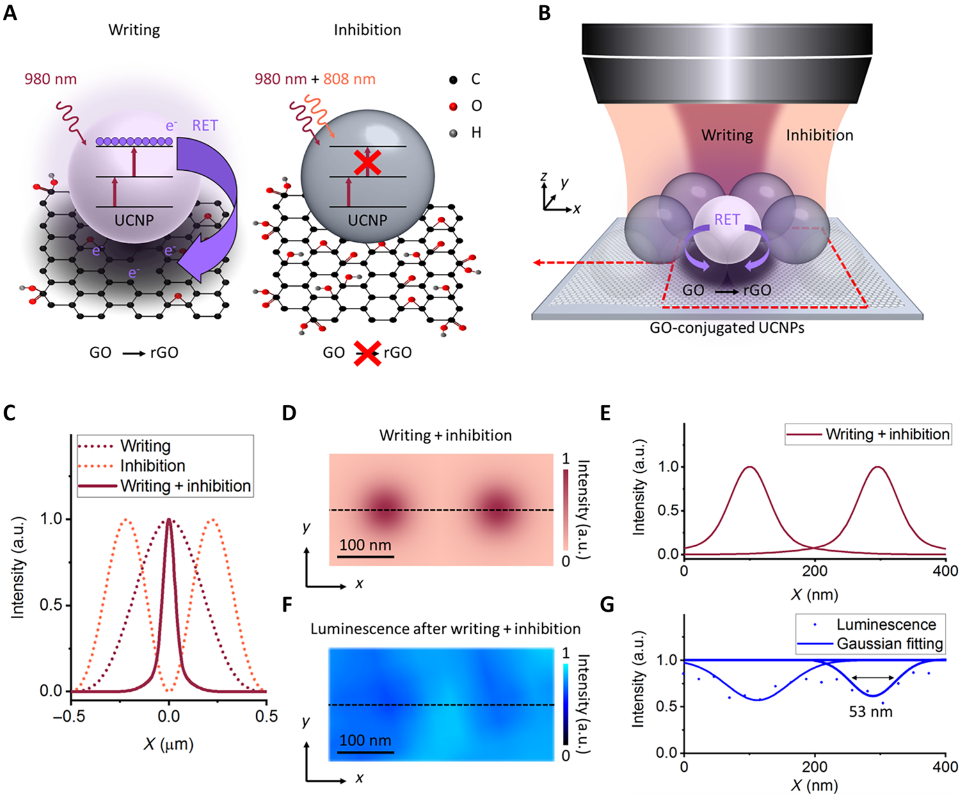

Fig. 1. Principle of nanoscale RETA optical writing on a GO-conjugated UCNP nanocomposite. (**A**) The writing beam induces GO reduction through RET of high-energy quanta from UCNPs, while the inhibition beam inhibits GO reduction through suppression of high-energy quantum generation in UCNPs. (**B**) The experimental setup of a dual-beam super-resolution configuration that enables writing of subdiffraction features on the nanocomposite. (**C**) Simulated intensity distribution of the 980-nm writing beam with a Gaussian shape (writing), the 808-nm inhibition beam with a doughnut shape (inhibition), and their spatial overlap (writing + inhibition) along the radial direction in the focal plane. (**D**) Simulated intensity distribution on the nanocomposite irradiated with the dual-beam super-resolution configuration (writing + inhibition) with a writing beam intensity of 0.13 MW cm^{-2} and an inhibition beam intensity of 11.25 MW cm^{-2}. (**E**) Simulated intensity profile along the dashed line in (D). (**F**) The 450-nm upconversion luminescence emission intensity from the nanocomposite after irradiation with the dual-beam super-resolution configuration (writing + inhibition). (**G**) Intensity profile along the dashed line in (F). a.u., arbitrary units.

features were characterized through fluorescence quenching microscopy combined with UCNP-enabled STED microscopy. The line profile analysis showed a lateral feature size after deconvolution and Gaussian fitting of ~50 nm (1/20th of the wavelength) for a writing beam intensity of 0.13 MW cm^{-2} and an inhibition beam intensity of 11.25 MW cm^{-2} (Fig. 1, F and G).

The key to achieving nanoscale RETA optical writing was to develop UCNPs capable of inducing localized and efficient GO reduction, which occurs over the energy threshold of 3.2 eV (corresponding to photons with the wavelength of 387 nm) (*27*). For this purpose, we synthesized hexagonal-phase Yb(30%)/Tm(4%) codoped $NaYF_4$ UCNPs with an average diameter of 24 nm (figs. S2 and S3). This size guarantees high spatial confinement for efficient RET, which occurs within a few nanometers, and enhanced optical resolution. Furthermore, the UCNPs showed efficient depletion of upconversion emission under dual-beam irradiation (figs. S4 to S7). This feature indicates that the high-energy quantum generation in the UCNPs can be prevented and, thus, enables inhibition of RETA optical writing. Differently from reported highly doped UCNPs with ~20% doping of Yb^{3+} that exhibit a low intensity of high-energy upconversion emission (*21*, *22*), our UCNPs had increased doping of Yb^{3+} sensitizer up to 30% along with Tm^{3+} emitter to enhance the absorption cross section of the UCNPs for intense upconversion to the $^1D_2$ and $^1I_6$ levels of Tm^{3+}. As a result, the UCNPs showed intense upconversion emission bands at 345 and 360 nm (corresponding to photons with the energy of 3.6 and 3.4 eV, respectively) upon 980-nm excitation (figs. S8 to S10). This upconversion emission spectrum resulted in a strong overlapping with the absorption spectrum of GO (spectral overlapping $J = 2.7 \times 10^{15}$ nm^4 M^{-1} cm^{-1}) (fig. S11) and a RET efficiency E_{RET} of ~83% (figs. S12 and S13), yielding an ideal condition for RETA optical writing.

The nanocomposite based on UCNPs conjugated with GO was prepared by placing a monolayer thin film of single UCNPs on single-layer GO nanosheets through controlled electrostatic self-assembly (Fig. 2A and figs. S14 to S16). This facile and scalable configuration ensures proximity of the UCNPs to GO nanosheets and dissipation of deleterious photo-generated heat. Two-color confocal microscopy imaging of the resulting nanocomposite was performed by recording upconversion emission at 450 nm from UCNPs upon 980-nm excitation and two-photon excitation (TPE) fluorescence at 650 nm from GO upon 880-nm excitation (Fig. 2B). Our results showed large-scale uniformity and superb control over the two components of the nanocomposite. It is well known that GO reduction results in an increased absorption coefficient, which enables quenching of nearby fluorophores and decreased TPE fluorescence because of elimination of oxygen-containing groups and varied sp^2

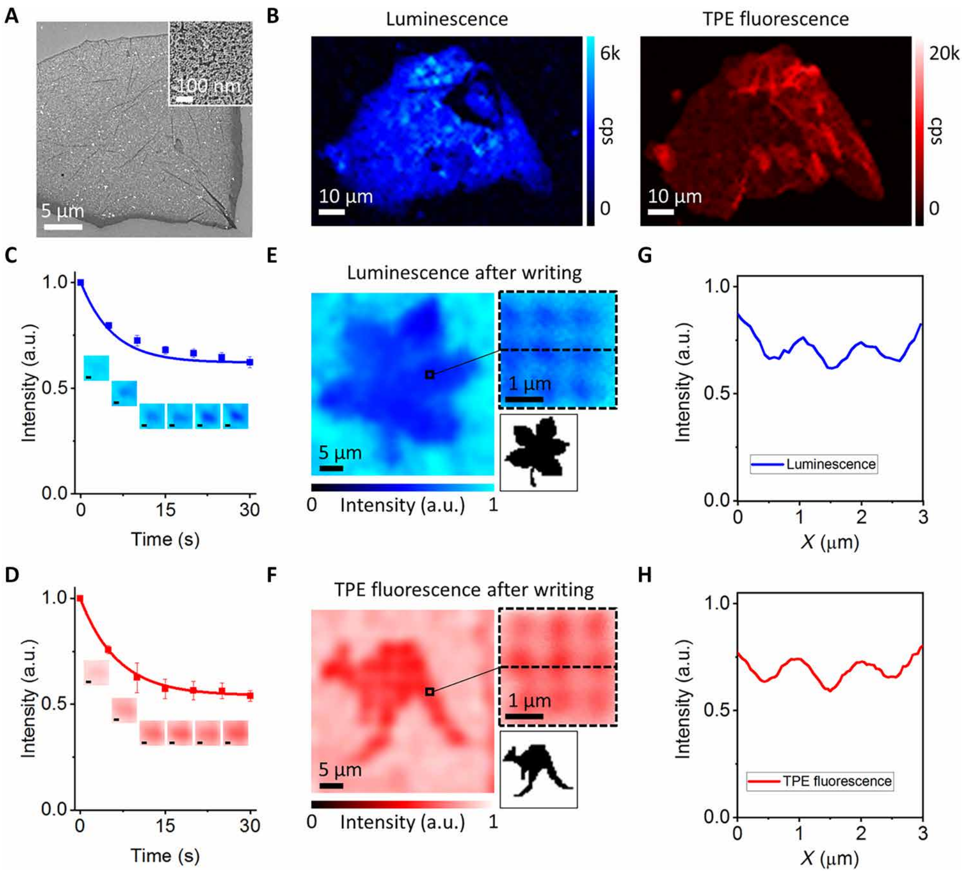

Fig. 2. RETA optical writing and dual-channel characterization. (**A**) Scanning electron microscopy (SEM) imaging of the nanocomposite based on the UCNPs conjugated with a GO flake. Inset: High-resolution SEM imaging of the nanocomposite. (**B**) Two-color confocal imaging of the nanocomposite, recording upconversion emission from the UCNPs (left) and TPE fluorescence from the GO flake (right). (**C** and **D**) Time-dependent measurements of upconversion emission and TPE fluorescence during RETA optical writing. Insets: Dual-channel characterization of single features through upconversion emission quenching and TPE fluorescence damping. Scale bar, 200 nm. (**E** and **F**) Upconversion emission and TPE fluorescence raster scans of patterns of features fabricated through RETA optical writing. Insets: High-magnification images of 3 × 3 features and the original photos reproduced in the patterns. (**G** and **H**) Intensity profiles along the dashed lines in the insets of (E) and (F).

and sp^3 hybridizations (*28*). We exploited these two phenomena as characterization tools to investigate the dynamics of UCNP-induced GO reduction during RETA optical writing (fig. S17). Time-dependent measurements indicated ~40% quenching of upconversion emission and ~50% decrease in TPE fluorescence after 30 s of irradiation of the nanocomposite with a writing beam intensity of 0.13 MW cm^{-2} (Fig. 2, C and D, and fig. S18). The amount of high-energy quanta generated in the UCNPs was estimated to be of 1.6×10^{23} quanta cm^{-2}. This value matches with that reported for GO reduction under UV irradiation (*27*) and provides evidence of UCNP-induced GO reduction during RETA optical writing.

The proposed mechanism for UCNP-induced GO reduction is reported as follows (Eq. 1)

$$\text{UCNPs–GO} + h\nu \rightarrow \text{UCNPs*–GO} \xrightarrow{\text{RET}} \text{UCNPs–GO*} \rightarrow \text{UCNPs–rGO} \tag{1}$$

where h is Planck's constant and ν is the frequency of the excitation at a wavelength of 980 nm. Irradiation of the nanocomposite (UCNPs–GO) by the writing beam causes excitation of the UCNPs (UCNPs*–GO) and generation of high-energy quanta through upconversion to the $^1D_2$ and $^1I_6$ levels of Tm^{3+}. For the GO-conjugated UCNPs, the energy match between these energy levels and the π orbital of GO results in strong orbital overlapping (fig. S19). Thus, RET from the UCNPs to GO (UCNPs–GO*) provides the energy required for activation of oxygen groups such as hydroxyl (O─H, 0.7 eV), epoxy (C─O─C, 1.9 to 2.1 eV), carbonyl (C═O, 3 to 4 eV), and carboxyl (COOH, 3 to 4 eV) groups, which results in GO reduction to rGO (UCNPs–rGO).

Figure 2 (E and F) shows raster scans of patterns comprising 50 × 50 features with a spacing of 0.97 μm fabricated in the nanocomposite through RETA optical writing. The patterns reproduce photos of a leaf and a kangaroo, which were retrieved through detection of the quenching of upconversion emission and the decrease in TPE fluorescence, respectively. The contrast of the features was defined as $|I_i - I_f|/I_i$, where I_i and I_f were the signal intensity before (initial) and after (final) RETA optical writing, respectively. The features had an average size of ~480 nm (Fig. 2, G and H), which well agrees with the expected diffraction limit of the wavelength of the writing beam. Considering the uniform coverage of the UCNPs on GO nanosheets, we estimated that ~300 UCNPs contributed to GO reduction for each feature.

Figure 3A shows the inhibition of RETA optical writing in the nanocomposite. Patterns comprising 50 × 50 features with a spacing of

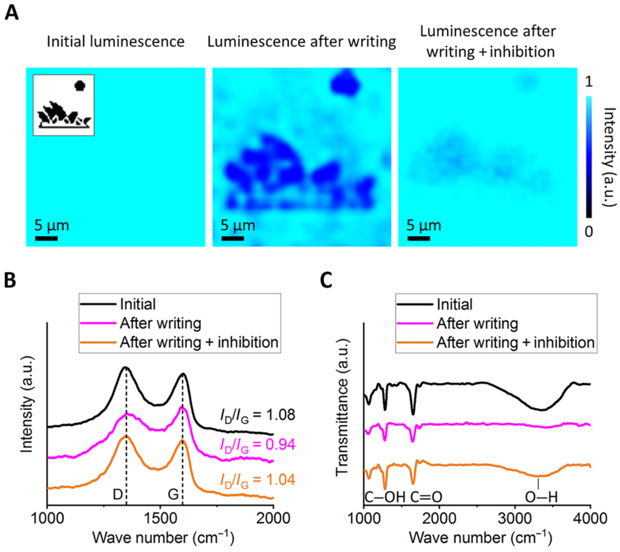

Fig. 3. Inhibition of RETA optical writing under dual-beam irradiation. (**A**) Selective inhibition of UCNP-induced GO reduction under dual-beam irradiation. Inset: The original photo reproduced in the patterns. (**B**) Raman spectroscopy and (**C**) FTIR spectroscopy of the nanocomposite at the initial stage, after writing and after writing + inhibition of features through UCNP-induced GO reduction.

0.97 μm and a reproduced photo of the Sydney Opera House were fabricated through irradiation with the writing beam and through co-irradiation with the writing and inhibition beams spatially coincident. Fluorescence quenching microscopy of the resulting features showed quenching of upconversion emission from the UCNPs after irradiation with the writing beam, which verifies GO reduction. By contrast, the intensity of the signal did not change noticeably after co-irradiation with the inhibition beam, which demonstrates inhibition of GO reduction. Raman spectroscopy of the nanocomposite showed two broad peaks at 1353 and 1605 cm^{-1}, which correspond to the D and G bands of GO, respectively (Fig. 3B). After irradiation with the writing beam, the ratio between the intensity of the D and G bands (I_D/I_G)—which relates to the number of defects in the material due to GO reduction—varied from 1.08 to 0.94, whereas after co-irradiation with the inhibition beam, the difference was negligible. Fourier transform infrared (FTIR) spectroscopy confirmed further evidence of the ability to inhibit GO reduction (Fig. 3C). After irradiation with the writing beam, the peak intensities of O—H bonds (3000 to 3700 cm^{-1}), C═O bonds (1730 cm^{-1}), and C—OH bonds (1220 to 1230 cm^{-1}) decreased compared with those measured at the initial state. By contrast, minor variations were noticed after co-irradiation with the inhibition beam.

To study RETA optical writing at the nanoscale under dual-beam super-resolution irradiation, we carried out steady-state modeling based on differential rate equations for the UCNP-GO system (fig. S20). In our model, irradiation of the nanocomposite with the

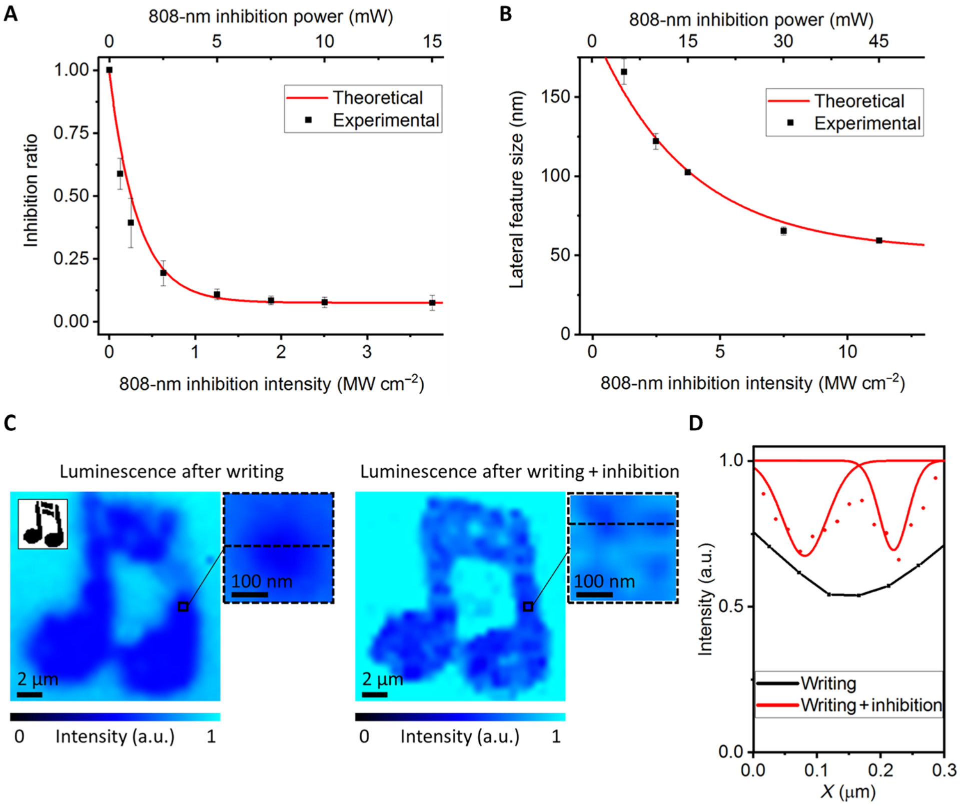

Fig. 4. Nanoscale RETA optical writing. (**A**) Inhibition of high-energy quantum generation in the GO-conjugated UCNPs under dual-beam irradiation with increasing intensity of the inhibition beam. (**B**) Lateral feature size under dual-beam super-resolution irradiation with increasing intensity of the inhibition beam. (**C**) Readout after diffraction-limited (left) and nanoscale (right) RETA optical writing of patterns. Insets: Magnified images of 2 × 2 features and the original photo reproduced in the patterns. (**D**) Intensity profiles along the dashed lines in the insets of (C) (black, diffraction limited; red, nanoscale).

writing beam induces GO reduction through RET of high-energy quanta generated in the UCNPs, whereas co-irradiation with the inhibition beam inhibits GO reduction by preventing high-energy quantum generation. We experimentally confirmed the theoretical predictions by achieving inhibition with an efficiency of ~95% and saturation intensity I_{sat} of ~250 kW cm^{-2} under dual-beam irradiation (Fig. 4A and figs. S21 to S23). In comparison, other photoinhibition methods through photoluminescence (*6*, *7*), STED (*8*), photodeactivation (*9*, *10*), photoradical generation (*11*–*13*), and photoabsorption (*14*) typically require inhibition beam intensities to achieve saturation between ~10^4 and ~10^7 W cm^{-2}, while photoinhibition methods through photochromism and photoswitching (*29*–*33*) require inhibition beam intensities to achieve saturation between ~1 and ~10^3 W cm^{-2} because of their inherently low saturation threshold.

These results facilitated the generation of subdiffraction features in the nanocomposite using a dual-beam super-resolution configuration (Fig. 4B and figs. S24 to S26). Figure 4C shows the comparison between two raster scans of patterns of features reproducing a photo of a musical note, which were retrieved through fluorescence quenching microscopy. The patterns comprising 50 × 50 features with a spacing of 195 nm were fabricated in the nanocomposite through RETA optical writing using a conventional confocal single-beam (writing) configuration and a dual-beam super-resolution (writing + inhibition) configuration. Whereas the confocal configuration blurred the features, a dual-beam super-resolution configuration enabled RETA optical writing of features with a lateral feature size of 54 nm after deconvolution and Gaussian fitting. This value corresponds to the use of only two UCNPs to induce GO reduction through RET (Fig. 4D). These results lay the foundation for nanoscale all-optical memory where individual GO-conjugated UCNPs are used for writing nanoscale optical data bits through localized GO reduction. The formed rGO enhances the quenching of upconversion emission from the adjacent UCNPs, hence the basis for reading subdiffraction optical data bits. Because upconversion based on multiphoton absorption nonlinearly depends on the intensity of the excitation beam (*34*), GO-conjugated UCNPs can be used to confine optical writing to small voxels within the focus of the objective.

DISCUSSION

Considering a lateral separation and axial separation of 2.5 times and 8 times the achieved lateral feature size (*4*), we estimate that this scheme enables a projected maximal DVD-sized single-disc data storage capacity approaching 700 TB. Furthermore, upconversion RET requires 10^4-fold lower beam intensity for writing of optical data bits compared with the nanostructuring of fused quartz glass (*2*, *3*). In principle, enhancing high-energy upconversion in UCNPs (*35*–*39*) and tuning the content of oxygen functional groups in GO (*40*) enable up to 10^4-fold improved writing efficiency for exposure times of milliseconds and energy consumption of microjoules per bit. Multifocal array techniques (*41*–*45*) enable throughputs of up to ~2.3 Gbps by detecting 450-nm upconversion luminescence (*46*). The restoration of the oxygen-containing groups in rGO through oxidation might allow multiple writing/readout cycles for rewritable memory. Selecting thermodynamically stable GO (*47*–*51*) and embedding the nanocomposite into a protective matrix (*52*–*56*) enable prolonged stability of the written features. The use of GO-conjugated UCNP-based optical memories with high capacity and low-power consumption is thus convenient for tackling growing demands for a sustainable data storage strategy in the Data Age.

MATERIALS AND METHODS

Reagents

Yttrium (III) acetate hydrate (99.9%), ytterbium (III) acetate tetrahydrate (99.9%), thulium (III) acetate hydrate (99.9%), sodium hydroxide (>98%), ammonium fluoride (>98%), 1-octadecene (90%), oleic acid (OA) (90%), and GO (2 mg ml^{-1}) in water solution were purchased from Sigma-Aldrich. All chemicals were used as received without further purification.

Synthesis of Yb/Tm co-doped $NaYF_4$ UCNPs

The Yb/Tm co-doped $NaYF_4$ UCNPs were synthesized through the widely used coprecipitation method (*57*). The typical inorganic crystalline matrix $NaYF_4$ was selected to host the Yb^{3+} and Tm^{3+} ions to guarantee intense upconversion emission and chemical stability of UCNPs. The OA ligand was removed from the surface of UCNPs for water dispensability.

Synthesis of $NaYF_4$:Yb/Tm (30%, X%, X = 1, 2, 4, 6, and 8) UCNPs

For the synthesis of the $NaYF_4$:Yb/Tm (30%, X%, X = 1, 2, 4, 6, and 8) UCNPs, 2 ml of $RE(CH_3CO_2)_3$ (0.4 mM, RE = Y, Yb, and Tm) in water was poured into a 50-ml flask containing 3 ml of OA and 7 ml of 1-octadecene. The mixture was heated at 150°C for 1.5 hours to promote the formation of the RE-oleate complexes and subsequently allowed to cool to 50°C. Then, 6 ml of methanol solution with NH_4F (1.6 mM) and NaOH (1 mM) was poured into the flask, and the resulting solution was stirred for 30 min. The temperature was then raised to 100°C to prompt the evaporation of methanol. After degassing for 20 min, the resulting mixture was heated to 290°C, maintained under a flow of nitrogen for 2 hours, and cooled to room temperature. The as-synthesized Yb/Tm co-doped $NaYF_4$ UCNPs were collected via centrifugation, washed with cyclohexane and ethanol, and, lastly, redispersed in cyclohexane (4 ml).

Synthesis of hydrophilic UCNPs by removing OA ligand

UCNPs capped with OA were dispersed in a 2 ml of HCl solution (0.1 M) and ultrasonicated for 15 min to allow removal of the surface ligands. After that, UCNPs were collected via centrifugation at 16,500 rpm for 20 min and purified by addition of an acidic ethanol solution (pH 4; prepared by mixing 0.1 M HCl aqueous solution with absolute ethanol). Ethanol and deionized water were used to wash UCNPs several times, which were then redispersed in deionized water.

Preparation of a nanocomposite based on UNCPs conjugated with GO

The preparation of a nanocomposite based on UCNPs conjugated with GO consisted of two steps:

- Step 1: Deposition of single-layer GO nanosheets onto indium tin oxide (ITO)–coated coverslip;
- Step 2: Self-assembly of single UCNPs onto single-layer GO nanosheets.

Step 1: Deposition of single-layer GO nanosheets onto ITO-coated coverslip

Single-layer GO nanosheets were deposited from water solution onto precleaned and salinized ITO-coated coverslip. The substrates were immersed in acetone for 2 min and allowed to dry to ensure the absence of oil or water. The silane solution was prepared by mixing 200 μl of 3-triethoxysilylpropylamine solution (Sigma-Aldrich, [3-aminopropyl]triethoxysilane 99%) with 5 ml of acetone, obtaining a 2% solution. The clean and dry substrates were dipped into the silane solution for 2 min. The silane reacted with the OH groups of the coverslip, linking aminoalkyl groups to it through covalent bonds. The resulting surface promoted the attachment of single-layer GO nanosheets to the coverslip. The substrates were washed with deionized water and allowed to dry. Single-layer GO nanosheets were deposited onto salinized ITO-coated coverslip by immersing each substrate into a water solution of GO at a concentration of 10 μg ml^{-1} for 5 s and then into a flask with deionized water for 30 s and, lastly, air dried.

Step 2: Self-assembly of single UCNPs onto single-layer GO nanosheets

Self-assembly was obtained by exploiting the electrostatic attraction between positively charged UCNPs and negatively charged GO nanosheets in an aqueous environment. Briefly, 100 μl of 0.1 μM UCNP solution was placed onto the ITO-coated coverslip, where single-layer GO nanosheets were previously deposited, according to Step 1. The solution was kept for 30 min to enable self-assembly of UCNPs onto the single-layer GO nanosheets. Then, the substrate was rinsed with deionized water to eliminate the excess of UCNP solution. By tuning the concentration of UCNPs in water and the deposition time, the areal density of the layer of self-assembled UCNPs could be controlled accurately. UCNPs deposited prevalently onto the GO nanosheets with negligible residue onto the substrate because of the electrostatic repulsion between UCNPs and silane groups previously formed onto the ITO-coated coverslip.

Characterization

Transmission electron microscopy (TEM) was performed using a JEOL 1010 TEM (2001) at an accelerating voltage of 100 kV equipped with Gatan Orius SC600 CCD Camera (2014). X-ray powder diffraction (XRD) patterns were obtained on a Bruker AXS D4 Endeavor wide-angle XRD instrument with a Cu Kα radiation source at $\lambda = 1.54056$ Å. Upconversion emission spectra were analyzed using an Andor Shamrock SR-500i imaging spectrometer equipped with an iXon EMCCD Camera using a CW laser at the wavelength of 980 nm (Thorlabs, BL976-PAG900) as a near-infrared light source at a power of 1 mW. UV-visible absorption spectra were collected by using an Agilent Cary 60 UV-Vis Spectrophotometer. The morphology analysis of the samples was carried out with an FEI Verios 460L field emission gun scanning electron microscopy at an accelerating voltage of 3 kV. Atomic force microscopy imaging was conducted with a Bruker Dimension Icon. An 80-MHz Ti:sapphire femtosecond laser (Coherent, Chameleon Ultra II) tuned at the wavelength of 880 nm was used as the excitation source for TPE fluorescence imaging of the nanocomposite. A mercury light source (Olympus, U-LH100HG) was used to photochemically reduce the GO in water solution. Unless otherwise noted, characterizations of the synthesized materials were performed at room temperature.

Dual-beam super-resolution optical system setup

The dual-beam super-resolution optical system setup was built on the basis of a custom-made confocal microscopy system. The samples were placed on a computer-controlled high-precision nanopositioning system based on a three-axis piezostage (Physik Instrumente, P-562.3CD). A beam at the wavelength of 980 nm from a CW laser (Thorlabs, BL976-PAG900) was used for excitation of UCNPs. After being collimated, the beam at the wavelength of 980 nm passed through two long-pass dichroic mirrors and was focused onto the sample by an oil immersion objective lens (Olympus, MPLAPON100XO2). The first dichroic mirror DC1 (Semrock, FF850-Di01-t1-25x36) also allowed a collimated 808-nm CW laser (Lumics, LU0808M250) for depletion of UCNPs to be combined with a 980-nm CW laser. The upconversion emission was collected by the same objective, separated from the beams at the wavelengths of 980 and 808 nm by the second dichroic mirror DC2 (Semrock, FF705-Di01-25x36), and coupled into a multimode fiber (Thorlabs, FG050LGA), which was connected to a single-photon avalanche diode (SPAD) (Excelitas Technologies, SPCM-AQRH-14-FC). A bandpass filter (Semrock, FF01-442/46-25) and a short pass filter (Semrock, FF02-694/SP-25) were inserted in the detection pathway to select the upconversion emission bands for imaging and measurements of the lifetime. A flipping mirror was also inserted to couple the signal with a spectrometer (Andor Shamrock SR-500i imaging spectrometer equipped with iXon EMCCD camera) for acquisition of upconversion emission spectra. For super-resolution imaging, a quarter waveplate (Thorlabs, WPQ10M-808) was used to convert the beam at the wavelength of 808 nm into circular polarized. A half waveplate (Newport, 10RP52-2) was also used to optimize the quality of the circular polarization and control the power of the beams in combination with Glan-Thompson prisms (Thorlabs, GTH10-A and GTH10-B). Last, a vortex phase plate (RPC Photonics, VPP-1a) was placed in the path of the 808-nm beam to generate a doughnut-shaped point spread function in the focal plane.

Upconversion emission lifetime measurement setup

For the measurements of upconversion emission lifetime, the beam at the wavelength of 980 nm from a CW laser (Thorlabs, BL976-PAG900) was modulated using an acousto-optic modulator (AOM) (AA OPTO-ELECTRONIC, MT110-A1-VIS/IR/1064) for 50-μs pulses with a frequency of 100 Hz for excitation of upconversion emission. The emitted photons went through a bandpass filter (Semrock, FF01-442/46-25) and a short pass filter (Semrock, FF02-694/SP-25) and were detected by a SPAD (Excelitas Technologies, SPCM-AQRH-14-FC). The trigger signal from the AOM was synchronized with the SPAD using a data acquisition (DAQ) card (National Instruments, cDAQ-9171). The effective emission decay time, τ_{eff}, was calculated by

$$\tau_{\mathrm{eff}} = \frac{1}{I_0}\int_0^{\infty} I(t)\, dt \qquad (2)$$

where $I(t)$ denotes the emission intensity as a function of time, t and I_0 represents the maximum emission intensity. The RET efficiency, E_{RET}, was derived from the upconversion emission lifetime measurements and calculated as

$$E_{\mathrm{RET}} = 1 - \frac{\tau_{\mathrm{DA}}}{\tau_{\mathrm{D}}} \qquad (3)$$

where τ_{DA} and τ_{D} are the lifetime of the donor (UCNPs) in the presence and absence of the acceptor (GO), respectively.

Determination of the spectral overlap integral *J*

The spectral overlap integral *J* of the RET pair comprising UCNPs and GO was calculated using the software FluorTools a|e. The wavelength range between 200 and 600 nm was evaluated. For

GO, the maximum absorption coefficient was estimated to be 180,000 L M^{-1} cm^{-1}.

Temperature rise in GO under irradiation with a CW laser

The temperature rise in GO under irradiation with a CW laser produces photothermal GO reduction (*58*), causing uncontrolled photodamage of GO and thus preventing nanoscale optical data writing and readout. A single-layer configuration of GO nanosheets was adopted to ensure efficient heat dissipation to the surrounding environment and avoid deleterious temperature increase in the sample. The temperature rise in a single-layer GO nanosheet under irradiation with a CW laser was estimated on the basis of a theoretical model that relies on an energy balance argument (*59*). The steady-state thermal increase ΔT experienced by a single-layer GO nanosheet upon absorbing irradiation of a CW laser is

$$\Delta T = \frac{I \cdot (1 - 10^{-A_\lambda})}{(h_{\mathrm{air}} + h_{\mathrm{sub}})} \tag{4}$$

where I is the intensity of the incident beam, A_λ is the absorbance at the irradiation wavelength, and h_{air} and h_{sub} are the interfacial thermal conductance between GO and the surrounding air and substrate, respectively. Specifically, the absorbance of a single-layer GO nanosheet under irradiation at the wavelengths of 980 and 800 nm was estimated to be $A_{980} = 3 \times 10^{-4}$ and $A_{808} = 5 \times 10^{-4}$, respectively (*58*). Because the values of h_{air} and h_{sub} for single-layer GO nanosheets are not available in the literature, estimations have been undertaken using the values for graphene (*60*)—h_{air} ~1×10^5 W m^{-2} K^{-1} and h_{sub} ~5×10^7 W m^{-2} K^{-1} for silica (SiO$_2$) and coverslip. Furthermore, because of $h_{\mathrm{air}} \ll h_{\mathrm{sub}}$, Eq. 4 can be simplified as follows

$$\Delta T \cong \frac{I \cdot (1 - 10^{-A_\lambda})}{h_{\mathrm{sub}}} \tag{5}$$

The photothermal GO reduction has been reported at a temperature of ~230°C (*61*); therefore, this study considered that $\Delta T = 200$ K can produce a photothermal reduction of a single-layer GO nanosheet initially at room temperature. The estimated intensity yielding $\Delta T = 200$ K from room temperature in a single-layer GO nanosheet deposited onto ITO-coated coverslip was several orders of magnitude higher than that of the beams at the wavelengths of 980 and 808 nm used throughout this research, and therefore, the photothermal GO reduction was considered negligible. The thermal increase in the sample strongly depends on the properties of heat dissipation of the substrate onto which the single-layer GO nanosheet was deposited. In this context, ITO-coated coverslip offered efficient heat dissipation away from GO, preventing thermal increase under the considered conditions.

Modeling upconversion and RET in GO-conjugated UCNPs under dual-beam irradiation

The model describing upconversion and RET in the GO-conjugated UCNPs under dual-beam irradiation was built considering that only the transfer of high-energy quanta from the $^1D_2$ and $^1I_6$ levels of Tm^{3+} to GO is efficient. The optical bandgap of GO is typically in the range from 2.7 to 3.5 eV (*62*, *63*) and corresponds to a larger energy gap than the $^1G_4$ energy level and lower energy levels of Tm^{3+} to the $^3H_6$ ground state. Furthermore, spectroscopy evidence shows a much weaker absorption of GO at longer upconversion emission wavelengths compared with the UV upconversion emission generated from the $^1D_2$ and $^1I_6$ levels. Under the assumption of fast nonradiative decay for the $^3H_5 \rightarrow {}^3F_4$ and $^3F_{2,3} \rightarrow {}^3H_4$ transitions, and thus combining each pair of energy levels into a single level, the following set of rate equations was established.

For Yb^{3+} ions:

- Yb^{3+} ($^2F_{7/2}$), ground-state n_{S1}

$$\frac{dn_{S1}}{dt} = -\frac{dn_{S2}}{dt} \tag{6}$$

- Yb^{3+} ($^2F_{5/2}$), excited-state n_{S2}

$$\frac{dn_{S2}}{dt} = P_{980} n_{S1} - W_s n_{S2} - (c_1 n_1 + c_2 n_2 + c_3 n_3 + (1 - \mathrm{ET}_{n5}) \\ c_4 n_4 + (1 - \mathrm{ET}_{n6}) c_5 n_5) n_{S2} \tag{7}$$

For Tm^{3+} ions:

- Tm^{3+} ($^3H_6$), ground-state n_1

$$\frac{dn_1}{dt} = -\sum_{i=2}^{6} \frac{dn_i}{dt} \tag{8}$$

- Tm^{3+} ($^3F_4$, $^3H_5$), excited-state n_2

$$\frac{dn_2}{dt} = c_1 n_{S2} n_1 - c_2 n_{S2} n_2 - W_2 n_2 + b_{32} W_3 n_3 + b_{42} W_4 n_4 + b_{52} \\ (1 - \mathrm{ET}_{n5}) W_5 n_5 + b_{62}(1 - \mathrm{ET}_{n6}) W_6 n_6 + 2 k_{31} n_1 n_3 + k_{41} n_1 n_4 \tag{9}$$

- Tm^{3+} ($^3H_4$, $^3F_{2,3}$), excited-state n_3

$$\frac{dn_3}{dt} = P_{808}(n_1 - n_3) + c_2 n_{S2} n_2 - c_3 n_{S2} n_3 - W_3 n_3 + b_{43} W_4 n_4 + b_{53} \\ (1 - \mathrm{ET}_{n5}) W_5 n_5 + b_{63}(1 - \mathrm{ET}_{n6}) W_6 n_6 - k_{31} \mathrm{n}_1 n_3 + \\ k_{41} n_1 n_4 + 2 k_{51} n_1 n_5 \tag{10}$$

- Tm^{3+} ($^1G_4$), excited-state n_4

$$\frac{dn_4}{dt} = c_3 n_{S2} n_3 - (1 - \mathrm{ET}_{n5}) c_4 n_{S2} n_4 - W_4 n_4 + \\ b_{54}(1 - \mathrm{ET}_{n5}) W_5 n_5 + b_{64}(1 - \mathrm{ET}_{n6}) W_6 n_6 - k_{41} n_1 n_4 \tag{11}$$

- Tm^{3+} ($^1D_2$), excited-state n_5

$$\frac{dn_5}{dt} = (1 - \mathrm{ET}_{n5}) c_4 n_{S2} n_4 - (1 - \mathrm{ET}_{n6}) c_5 n_{S2} n_5 - (1 - \mathrm{ET}_{n5}) W_5 \\ n_5 + b_{65}(1 - \mathrm{ET}_{n6}) W_6 n_6 - k_{51} n_1 n_5 \tag{12}$$

- Tm^{3+} ($^1I_6$), excited-state n_6

$$\frac{dn_6}{dt} = (1 - \mathrm{ET}_{n6}) c_5 n_{S2} n_5 - (1 - \mathrm{ET}_{n6}) W_6 n_6 \tag{13}$$

For GO:

- GO, ground-state n_{GO1}

$$\frac{dn_{GO1}}{dt} = -\frac{dn_{GO2}}{dt} \tag{14}$$

- GO, excited-state n_{GO2}

$$\frac{dn_{GO2}}{dt} = ET_{n5} \frac{dn_5}{dt} + \mathrm{ET}_{n6} \frac{dn_6}{dt} - W_{GO2} n_{GO2} \tag{15}$$

where $P_{980} = \left(\frac{\sigma_{Yb} \lambda_{980} I_{980}}{hc}\right)$ is the excitation rate of Yb^{3+} under irradiation at the wavelength of 980 nm, and I_{980} is the intensity of the beam at the wavelength of 980 nm for excitation; $P_{808} = \left(\frac{\sigma_{STED} \lambda_{808} I_{808}}{hc}\right)$

is the absorption/stimulated emission rate of Tm^{3+} under irradiation at the wavelength of 808 nm, so that the term of $\left(\frac{\sigma_{STED}\lambda_{808}I_{808}}{hc}\right)$ $(n_1 - n_3)$ is the net effect of absorption/stimulated emission, and I_{808} is the intensity of the beam at the wavelength of 808 nm for depletion; σ_{Yb} is the absorption cross section of Yb^{3+} for the wavelength of 980 nm; σ_{STED} is the absorption/stimulated emission cross section of Tm^{3+} for the wavelength of 808 nm; λ_{980} is the wavelength of the beam for excitation; λ_{808} is the wavelength of the beam for depletion; h is Planck's constant; c is the light speed; W_s is the intrinsic decay rate of the excited Yb^{3+}; c_i is the upconversion coefficient between the excited Yb^{3+} and Tm^{3+} on level i; W_i is the intrinsic decay rate of Tm^{3+} on level i; b_{ij} is the branching ratio for Tm^{3+} decaying from level i to level j, satisfying $\sum_{j=1}^{i-1} b_{ij} = 1$; k_{ij} is the cross-relaxation coefficient between Tm^{3+} on level i and level j; ET_{ni} is the energy transfer from Tm^{3+} to GO; and n is the electronic population in a specific energy level fulfilling the following conditions

$$n_{S1} + n_{S2} = 1 \tag{16}$$

$$n_1 + n_2 + n_3 + n_4 + n_5 + n_6 = 1 \tag{17}$$

$$n_{GO1} + n_{GO2} = 1 \tag{18}$$

The model presented here involves parameters specific to the properties of UCNPs and GO. The reaction constants can be fixed, leaving only I_{980} and I_{808} as variables. To validate the model, a combination of highly doped Yb/Tm co-doped $NaYF_4$ UCNPs and GO was simulated using the parameters in table S1.

Simulated lateral feature size under dual-beam super-resolution irradiation

In dual-beam super-resolution optical techniques, such as STED microscopy, a Gaussian-shaped beam for excitation is spatially overlapped with a doughnut-shaped beam for depletion, thereby confining the effective point spread function to the center of the doughnut at the nanoscale. The model based on rate equations previously developed was used to determine the population of electrons in the energy levels of the GO-conjugated UCNPs. Thus, by simulating the distribution of the intensity of the beams at the wavelength of 980 nm for excitation and the wavelength of 808 nm for depletion in the focal region, it was possible to evaluate the lateral feature size under dual-beam super-resolution irradiation. This study considered a circularly polarized beam at the wavelength of 980 nm and a circularly polarized vortex beam at the wavelength of 808 nm generated by passing through a 2π vortex phase plate with a helical phase retardation from zero to 2π focused with a high NA objective lens. The electric field in the focal region was (*26*)

$$E(r,\varphi,z) = \begin{bmatrix} E_x \\ E_y \\ E_z \end{bmatrix} = -\frac{ikf}{2\pi}\int_0^{\alpha}\int_0^{2\pi} A(\theta)\exp(im\phi)\sin\theta\sqrt{\cos\theta}\times$$

$$\exp[ik(z\cos\theta + r\sin\theta\cos(\phi-\varphi))]\times \tag{19}$$

$$\begin{bmatrix} (\cos^2\phi\cos\theta + \sin^2\phi) \pm i\cos\phi\sin\phi(\cos\theta - 1) \\ \cos\phi\sin\phi(\cos\theta - 1) \pm i(\cos^2\phi + \sin^2\phi\cos\theta) \\ \sin\theta\exp(\pm i\phi) \end{bmatrix} d\theta\, d\phi$$

where r, φ, and z are the cylindrical coordinates; ϕ is the azimuthal angle of the incident beam; $k = 2\pi/\lambda$ is the wave vector; f is the focal length of the high NA objective; α is the maximal NA angle; and θ is the NA angle that varies between 0 and α. Assuming that the optical system is in free space (i.e., the index of refraction n is 1), the maximal angle α is $\alpha = \arcsin(NA/n)$, where n is the index of refraction of the material in the focal region, $A(\theta)$ is the pupil anodization function at the surface of the objective's aperture, and $\exp(im\phi)$ is the vortex phase factor of the incident beam. For the beam at the wavelength of 980 nm, $m = 0$, while for the beam at the wavelength of 808 nm passing through the 2π phase plate, $m = 1$. The symbol ± relates to the handedness of the circularly polarized beams. Right circular polarized beams were considered in this calculation. For the focal spot calculation, the considered NA for the objective lens was 1.4. Having established the depletion efficiency of upconversion emission at the wavelength of 450 nm in UCNP-only and GO-conjugated UCNPs under excitation at the wavelength of 980 nm and depletion at the wavelength of 808 nm, the intensity distribution in the focal region was determined by applying the vectorial Debye theory (*26*).

Calculation of high-energy quanta yielding GO reduction during RETA optical writing

The number of high-energy quanta generated through upconversion of the beam at the wavelength of 980 nm yielding GO reduction during RETA optical writing was estimated considering the corresponding total UV photon dose Φ associated with the photochemical GO reduction, calculated as

$$\Phi = I \times \left(\frac{\lambda}{hc}\right) \times t \tag{20}$$

where I is the intensity of the beam at the wavelength of 980 nm, λ is the irradiation wavelength, h is Plank's constant, c is the light speed, and t is the exposure time. For the considered experimental conditions (intensity of the beam at the wavelength of 980 nm I of 0.13 MW cm^{-2} and exposure time t of 30 s), the resulting photon dose Φ is of 1.9×10^{25} photons cm^{-2}. Furthermore, considering E_{RET} of ~83% for UCNP-GO pair and a typical UV conversion efficiency η^{UV} of ~1% for UCNPs, the number of the high-energy quanta yielding GO reduction was of 1.6×10^{23} quanta cm^{-2}.

Calculation of the optical bandgap for GO and rGO

The optical bandgap values for GO and rGO were calculated from the UV-visible absorption data using the Tauc relation

$$(\alpha h\nu)^n = K(h\nu - E_g) \tag{21}$$

where α is the absorption coefficient, $h\nu$ is the incident photon energy, E_g is the optical bandgap energy, and K is a constant. The parameter n is indicative of the nature of transition and for these samples is equal to ½. The optical bandgaps of GO and rGO were determined using a linear extrapolation to the Tauc plot as shown in fig. S28.

SUPPLEMENTARY MATERIALS

Supplementary material for this article is available at http://advances.sciencemag.org/cgi/content/full/7/9/eabe2209/DC1

REFERENCES AND NOTES

1. J. H. Strickler, W. W. Webb, Three-dimensional optical data storage in refractive media by two-photon point excitation. *Opt. Lett.* **16**, 1780–1782 (1991).

2. J. Zhang, M. Gecevičius, M. Beresna, P. G. Kazansky, Seemingly unlimited lifetime data storage in nanostructured glass. *Phys. Rev. Lett.* **112**, 033901 (2014).
3. J. Langston, Project Silica proof of concept stores Warner Bros. 'Superman' movie on quartz glass (2019); https://news.microsoft.com/innovation-stories/ignite-project-silica-superman/?utm_source=stories&utm_campaign=1639.
4. M. Gu, X. Li, Y. Cao, Optical storage arrays: A perspective for future big data storage. *Light: Sci. Appl.* **3**, e177 (2014).
5. M. Gu, Q. Zhang, S. Lamon, Nanomaterials for optical data storage. *Nat. Rev. Mater.* **1**, 16070 (2016).
6. J. Fischer, G. von Freymann, M. Wegener, The materials challenge in diffraction-unlimited direct-laser-writing optical lithography. *Adv. Mater.* **22**, 3578–3582 (2010).
7. J. Fischer, M. Wegener, Three-dimensional direct laser writing inspired by stimulated-emission-depletion microscopy. *Opt. Mater. Express* **1**, 614–624 (2011).
8. R. Wollhofen, J. Katzmann, C. Hrelescu, J. Jacak, T. A. Klar, 120 nm resolution and 55 nm structure size in STED-lithography. *Opt. Express* **21**, 10831–10840 (2013).
9. L. Li, R. R. Gattass, E. Gershgoren, H. Hwang, J. T. Fourkas, Achieving λ/20 resolution by one-color initiation and deactivation of polymerization. *Science* **324**, 910–913 (2009).
10. M. P. Stocker, L. Li, R. R. Gattass, J. T. Fourkas, Multiphoton photoresists giving nanoscale resolution that is inversely dependent on exposure time. *Nat. Chem.* **3**, 223–227 (2011).
11. T. F. Scott, B. A. Kowalski, A. C. Sullivan, C. N. Bowman, R. R. McLeod, Two-color single-photon photoinitiation and photoinhibition for subdiffraction photolithography. *Science* **324**, 913–917 (2009).
12. Y. Cao, Z. Gan, B. Jia, R. A. Evans, M. Gu, High-photosensitive resin for super-resolution direct-laser-writing based on photoinhibited polymerization. *Opt. Express* **19**, 19486–19494 (2011).
13. Z. Gan, Y. Cao, R. A. Evans, M. Gu, Three-dimensional deep sub-diffraction optical beam lithography with 9 nm feature size. *Nat. Commun.* **4**, 2061 (2013).
14. B. Harke, W. Dallari, G. Grancini, D. Fazzi, F. Brandi, A. Petrozza, A. Diaspro, Polymerization inhibition by triplet state absorption for nanoscale lithography. *Adv. Mater.* **25**, 904–909 (2013).
15. F. Auzel, Upconversion and anti-stokes processes with f and d ions in solids. *Chem. Rev.* **104**, 139–174 (2004).
16. Z. Chen, S. He, H.-J. Butt, S. Wu, Photon upconversion lithography: Patterning of biomaterials using near-infrared light. *Adv. Mater.* **27**, 2203–2206 (2015).
17. G. Chen, H. Qiu, P. N. Prasad, X. Chen, Upconversion nanoparticles: Design, nanochemistry, and applications in theranostics. *Chem. Rev.* **114**, 5161–5214 (2014).
18. J.-C. Boyer, C.-J. Carling, B. D. Gates, N. R. Branda, Two-way photoswitching using one type of near-infrared light, upconverting nanoparticles, and changing only the light intensity. *J. Am. Chem. Soc.* **132**, 15766–15772 (2010).
19. S. Chen, A. Z. Weitemier, X. Zeng, L. He, X. Wang, Y. Tao, A. J. Y. Huang, Y. Hashimotodani, M. Kano, H. Iwasaki, L. K. Parajuli, S. Okabe, D. B. L. Teh, A. H. All, I. Tsutsui-Kimura, K. F. Tanaka, X. Liu, T. J. McHugh, Near-infrared deep brain stimulation via upconversion nanoparticle–mediated optogenetics. *Science* **359**, 679–684 (2018).
20. K. Zheng, S. Han, X. Zeng, Y. Wu, S. Song, H. Zhang, X. Liu, Rewritable optical memory through high-registry orthogonal upconversion. *Adv. Mater.* **30**, 1801726 (2018).
21. Y. Liu, Y. Lu, X. Yang, X. Zheng, S. Wen, F. Wang, X. Vidal, J. Zhao, D. Liu, Z. Zhou, C. Ma, J. Zhou, J. A. Piper, P. Xi, D. Jin, Amplified stimulated emission in upconversion nanoparticles for super-resolution nanoscopy. *Nature* **543**, 229–233 (2017).
22. Q. Zhan, H. Liu, B. Wang, Q. Wu, R. Pu, C. Zhou, B. Huang, X. Peng, H. Ågren, S. He, Achieving high-efficiency emission depletion nanoscopy by employing cross relaxation in upconversion nanoparticles. *Nat. Commun.* **8**, 1058 (2017).
23. Y. Zhu, S. Murali, W. Cai, X. Li, J. W. Suk, J. R. Potts, R. S. Ruoff, Graphene and graphene oxide: Synthesis, properties, and applications. *Adv. Mater.* **22**, 3906–3924 (2010).
24. T. Förster, Zwischenmolekulare Energiewanderung und Fluoreszenz. *Ann. Phys.* **437**, 55–75 (1948).
25. Y. L. Zhang, L. Guo, H. Xia, Q. D. Chen, J. Feng, H. B. Sun, Photoreduction of graphene oxides: Methods, properties, and applications. *Adv. Opt. Mater.* **2**, 10–28 (2014).
26. M. Gu, *Advanced Optical Imaging Theory* (Springer Berlin, Berlin, 2013).
27. V. A. Smirnov, A. A. Arbuzov, Y. M. Shul'ga, S. A. Baskakov, V. M. Martynenko, V. E. Muradyan, E. I. Kresova, Photoreduction of graphite oxide. *High Energy Chem.* **45**, 57–61 (2011).
28. C. T. Chien, S. S. Li, W. J. Lai, Y. C. Yeh, H. A. Chen, I. S. Chen, L. C. Chen, K. H. Chen, T. Nemoto, S. Isoda, M. Chen, Tunable photoluminescence from graphene oxide. *Angew. Chem. Int. Ed.* **51**, 6662–6666 (2012).
29. T. L. Andrew, H.-Y. Tsai, R. Menon, Confining light to deep subwavelength dimensions to enable optical nanopatterning. *Science* **324**, 917–921 (2009).
30. H. Vijayamohanan, E. F. Palermo, C. K. Ullal, Spirothiopyran-based reversibly saturable photoresist. *Chem. Mater.* **29**, 4754–4760 (2017).
31. H. Vijayamohanan, G. S. Kenath, E. F. Palermo, C. K. Ullal, Super-resolution interference lithography enabled by non-equilibrium kinetics of photochromic monolayers. *RSC Adv.* **9**, 28841–28850 (2019).
32. T. Grotjohann, I. Testa, M. Leutenegger, H. Bock, N. T. Urban, F. Lavoie-Cardinal, K. I. Willig, C. Eggeling, S. Jakobs, S. W. Hell, Diffraction-unlimited all-optical imaging and writing with a photochromic GFP. *Nature* **478**, 204–208 (2011).
33. P. Mueller, M. M. Zieger, B. Richter, A. S. Quick, J. Fischer, J. B. Mueller, L. Zhou, G. U. Nienhaus, M. Bastmeyer, C. Barner-Kowollik, M. Wegener, Molecular switch for sub-diffraction laser lithography by photoenol intermediate-state cis–trans isomerization. *ACS Nano* **11**, 6396–6403 (2017).
34. M. Pollnau, D. R. Gamelin, S. R. Lüthi, H. U. Güdel, M. P. Hehlen, Power dependence of upconversion luminescence in lanthanide and transition-metal-ion systems. *Phys. Rev. B* **61**, 3337–3346 (2000).
35. P. Ramasamy, P. Chandra, S. W. Rheea, J. Kim, Enhanced upconversion luminescence in $NaGdF_4$:Yb,Er nanocrystals by Fe^{3+} doping and their application in bioimaging. *Nanoscale* **5**, 8711–8717 (2013).
36. J. Zhao, D. Jin, E. P. Schartner, Y. Lu, Y. Liu, A. V. Zvyagin, L. Zhang, J. M. Dawes, P. Xi, J. A. Piper, E. M. Goldys, T. M. Monro, Single-nanocrystal sensitivity achieved by enhanced upconversion luminescence. *Nat. Nanotechnol.* **8**, 729–734 (2013).
37. X. Chen, L. Jin, W. Kong, T. Sun, W. Zhang, X. Liu, J. Fan, S. F. Yu, F. Wang, Confining energy migration in upconversion nanoparticles towards deep ultraviolet lasing. *Nat. Commun.* **7**, 10304 (2016).
38. W. Zhang, F. Ding, S. Y. Chou, Large enhancement of upconversion luminescence of $NaYF_4$:Yb^{3+}/Er^{3+} nanocrystal by 3D plasmonic nano-antennas. *Adv. Mater.* **24**, OP236–OP241 (2012).
39. X. Zou, M. Xu, W. Yuan, Q. Wang, Y. Shi, W. Feng, F. Li, A water-dispersible dye-sensitized upconversion nanocomposite modified with phosphatidylcholine for lymphatic imaging. *Chem. Commun.* **52**, 13389–13392 (2016).
40. L. Luo, T. Peng, M. Yuan, H. Sun, S. Dai, L. Wang, Preparation of graphite oxide containing different oxygen-containing functional groups and the study of ammonia gas sensitivity. *Sensors* **18**, 3745 (2018).
41. X. Li, Y. Cao, N. Tian, L. Fu, M. Gu, Multifocal optical nanoscopy for big data recording at 30 TB capacity and gigabits/second data rate. *Optica* **2**, 567–570 (2015).
42. M. Gu, H. Lin, X. Li, Parallel multiphoton microscopy with cylindrically polarized multifocal arrays. *Opt. Lett.* **38**, 3627–3630 (2013).
43. X. Li, H. Ren, X. Chen, J. Liu, Q. Li, C. Li, G. Xue, J. Jia, L. Cao, A. Sahu, B. Hu, Y. Wang, G. Jin, M. Gu, Athermally photoreduced graphene oxides for three-dimensional holographic images. *Nat. Commun.* **6**, 6984 (2015).
44. A. Chmyrov, J. Keller, T. Grotjohann, M. Ratz, E. d'Este, S. Jakobs, C. Eggeling, S. W. Hell, Nanoscopy with more than 100,000 'doughnuts'. *Nat. Methods* **10**, 737–740 (2013).
45. Y. Xue, P. T. C. So, Three-dimensional super-resolution high-throughput imaging by structured illumination STED microscopy. *Opt. Express* **26**, 20920–20928 (2018).
46. P. Villanueva-Delgado, D. Biner, K. W. Krämer, Judd–Ofelt analysis of β-$NaGdF_4$: Yb^{3+}, Tm^{3+} and β-$NaGdF_4$: Er^{3+} single crystals. *J. Lumin.* **189**, 84–90 (2017).
47. J.-A. Yan, L. Xian, M. Y. Chou, Structural and electronic properties of oxidized graphene. *Phys. Rev. Lett.* **103**, 086802 (2009).
48. J.-A. Yan, M. Y. Chou, Oxidation functional groups on graphene: Structural and electronic properties. *Phys. Rev. B* **82**, 125403 (2010).
49. L. Wang, Y. Y. Sun, K. Lee, D. West, Z. F. Chen, J. J. Zhao, S. B. Zhang, Stability of graphene oxide phases from first-principles calculations. *Phys. Rev. B* **82**, 161406 (2010).
50. A. Bagri, C. Mattevi, M. Acik, Y. J. Chabal, M. Chhowalla, V. B. Shenoy, Structural evolution during the reduction of chemically derived graphene oxide. *Nat. Chem.* **2**, 581–587 (2010).
51. S. Zhou, A. Bongiorno, Origin of the chemical and kinetic stability of graphene oxide. *Sci. Rep.* **3**, 2484 (2013).
52. Q. Zhang, Z. Xia, Y.-B. Cheng, M. Gu, High-capacity optical long data memory based on enhanced Young's modulus in nanoplasmonic hybrid glass composites. *Nat. Commun.* **9**, 1183 (2018).
53. A. J. Glover, M. Cai, K. R. Overdeep, D. E. Kranbuehl, H. C. Schniepp, In situ reduction of graphene oxide in polymers. *Macromolecules* **44**, 9821–9829 (2011).
54. T. Ramanathan, A. A. Abdala, S. Stankovich, D. A. Dikin, M. Herrera-Alonso, R. D. Piner, D. H. Adamson, H. C. Schniepp, X. Chen, R. S. Ruoff, S. T. Nguyen, I. A. Aksay, R. K. Prud'Homme, L. C. Brinson, Functionalized graphene sheets for polymer nanocomposites. *Nat. Nanotechnol.* **3**, 327–331 (2008).
55. H. Kim, A. A. Abdala, C. W. Macosko, Graphene/polymer nanocomposites. *Macromolecules* **43**, 6515–6530 (2010).
56. S. Stankovich, D. A. Dikin, G. H. B. Dommett, K. M. Kohlhaas, E. J. Zimney, E. A. Stach, R. D. Piner, S. T. Nguyen, R. S. Ruoff, Graphene-based composite materials. *Nature* **442**, 282–286 (2006).
57. F. Wang, R. Deng, X. Liu, Preparation of core-shell $NaGdF_4$ nanoparticles doped with luminescent lanthanide ions to be used as upconversion-based probes. *Nat. Protoc.* **9**, 1634–1644 (2014).

58. Y. Zhou, Q. Bao, B. Varghese, L. A. L. Tang, C. K. Tan, C.-H. Sow, K. P. Loh, Microstructuring of graphene oxide nanosheets using direct laser writing. *Adv. Mater.* **22**, 67–71 (2010).
59. D. Wang, M. T. Carlson, H. H. Richardson, Absorption cross section and interfacial thermal conductance from an individual optically excited single-walled carbon nanotube. *ACS Nano* **5**, 7391–7396 (2011).
60. W. Cai, A. L. Moore, Y. Zhu, X. Li, S. Chen, L. Shi, R. S. Ruoff, Thermal transport in suspended and supported monolayer graphene grown by chemical vapor deposition. *Nano Lett.* **10**, 1645–1651 (2010).
61. D. A. Sokolov, C. M. Rouleau, D. B. Geohegan, T. M. Orlando, Excimer laser reduction and patterning of graphite oxide. *Carbon* **53**, 81–89 (2013).
62. M. A. Velasco-Soto, S. A. Pérez-García, J. Alvarez-Quintana, Y. Cao, L. Nyborg, L. Licea-Jiménez, Selective band gap manipulation of graphene oxide by its reduction with mild reagents. *Carbon* **93**, 967–973 (2015).
63. A. Mathkar, D. Tozier, P. Cox, P. Ong, C. Galande, K. Balakrishnan, A. L. M. Reddy, P. M. Ajayan, Controlled, stepwise reduction and band gap manipulation of graphene oxide. *J. Phys. Chem. Lett.* **3**, 986–991 (2012).
64. Y.-F. Wang, G.-Y. Liu, L.-D. Sun, J.-W. Xiao, J.-C. Zhou, C.-H. Yan, Nd^{3+}-sensitized upconversion nanophosphors: Efficient in vivo bioimaging probes with minimized heating effect. *ACS Nano* **7**, 7200–7206 (2013).
65. A. V. Smith, J. J. Smith, Mode instability thresholds for Tm-doped fiber amplifiers pumped at 790 nm. *Opt. Express* **24**, 975–992 (2016).
66. J. Shang, L. Ma, J. Li, W. Ai, T. Yu, G. G. Gurzadyan, The origin of fluorescence from graphene oxide. *Sci. Rep.* **2**, 792 (2012).
67. S. Kaniyankandy, S. N. Achary, S. Rawalekar, H. N. Ghosh, Ultrafast relaxation dynamics in graphene oxide: Evidence of electron trapping. *J. Phys. Chem. C* **115**, 19110–19116 (2011).

Acknowledgments: We acknowledge the facilities, and the scientific and technical assistance, of the Australian Microscopy & Microanalysis Research Facility at the RMIT Microscopy and Microanalysis Facility, at RMIT University. **Funding:** M.G. acknowledges the support from the Australian Research Council (Discovery Project DP170101775) and the funding support from the Zhangjiang National Innovation Demonstration Zone (ZJ2019-ZD-005). X.L. acknowledges the support from the Agency for Science, Technology and Research (A*STAR) (grant no. A1883c0011). Q.Z. acknowledges the funding support from the National Natural Science Foundation of China (61975123). **Author contributions:** S.L., Q.Z., and M.G. proposed the idea and conceptual and experimental design, and analyzed the data. X.L. and M.G. supervised the project and led the collaboration efforts. All authors were involved in the writing of the paper. S.L. completed the development of the rate equation model and related simulation, the characterization of materials as well as lifetime, spectroscopy, microscopy, and data storage experiments. S.L. and Q.Z. built the dual-beam super-resolution optical system setup and time-dependent emission spectroscopy setup. Y.W. synthesized and characterized the upconversion nanoparticles. **Competing interests:** The authors declare that they have no competing interests. **Data and materials availability:** All data needed to evaluate the conclusions in the paper are present in the paper and/or the Supplementary Materials and are archived on a laboratory computer at the Royal Melbourne Institute of Technology. Supplementary information is available for this paper. Correspondence and requests for materials should be addressed to M.G. (gumin@usst.edu.cn).

Submitted 7 August 2020
Accepted 5 January 2021
Published 24 February 2021
10.1126/sciadv.abe2209

Citation: S. Lamon, Y. Wu, Q. Zhang, X. Liu, M. Gu, Nanoscale optical writing through upconversion resonance energy transfer. *Sci. Adv.* **7**, eabe2209 (2021).